Templating growth of gold nanostructures with a CdSe quantum dot array

Neelima Paul,*[a] Ezzeldin Metwalli,[b] Yuan Yao,[b] Matthias Schwartzkopf,[c] Shun Yu,[c,d] Stephan V. Roth,[c] Peter Müller-Buschbaum[b] and Amitesh Paul*[e]

In optoelectronic devices based on quantum dot arrays, thin nanolayers of gold are preferred as stable metal contacts and for connecting recombination centers. The optimal morphology requirements are uniform arrays with precisely controlled positions and sizes over a large area with long range ordering since this strongly affects device performance. To understand the development of gold layer nano-morphology, the detailed mechanism of structure formation are probed with time-resolved grazing incidence small-angle X-ray scattering (GISAXS) during gold sputter deposition. Gold is sputtered on a CdSe quantum dot array with a characteristic quantum dot spacing of ≈7 nm. In the initial stages of gold nano-structure growth, a preferential deposition of gold on top of quantum dots occurs. Thus, the quantum dots act as nucleation sites for gold growth. In later stages, the gold nanoparticles surrounding the quantum dots undergo a coarsening to form a complete layer comprised of gold-dot clusters. Next, growth proceeds dominantly via vertical growth of gold on these gold-dot clusters to form an gold capping layer. In this capping layer, a shift of the cluster boundaries due to ripening is found. Thus, a templating of gold on a CdSe quantum dot array is feasible at low gold coverage.

Introduction

Quantum dots attract much interest because they exhibit size-dependent optical and electronic properties.[1,2] Semiconductor quantum dot arrays have several potential applications in nanoelectronics and optoelectronics, for example, in lasers, next generation solar cells, light emitting diodes, quantum computation.[3] For example, CdSe quantum dots are chemically stable and highly luminescent in the entire visible light range therefore several CdSe-based quantum dot solar cells have been fabricated during the recent years.[4–6] For the aforementioned optical applications, a sharp size distribution and a long range ordering of the quantum dots is beneficial, because this leads to a more uniform emission spectrum. However, there is only little information on ordering and correlation effects, which is desirable for many device applications.[7] It is to be noted that CdSe quantum dots are rather small, and

due to strong intermixing during overgrowth by other II–VI semiconductors they exhibit a diminished chemical contrast. Therefore, the detection of such rather weak compositional fluctuations and their correlation is experimentally challenging.[8] Gold has a sufficient chemical contrast to CdSe and therefore is a suitable material for overgrowth and for monitoring correlation effects of gold growth on CdSe quantum dot templates.

Growth of gold on electronically active materials like semiconductors is also of extreme interest in research involving field effect transistors, light emitting diodes and solar cells.[9–11] In the latter, the preferred metal contacts are usually gold, silver and aluminum. In conventional solar cells, the role of thin metallic films is to allow the easy passage for charge carriers whereas in tandem solar cells, they can also serve as charge recombination centers between the single junctions.[12,13] Thus, growth of metals such as gold on semiconductors and their mutual interactions are interesting from the viewpoint of electronic devices as well. Growth of gold nanostructures itself is relevant in various aspects of nanotechnology due to its size dependent properties.[14–17]

Observation of gold growth on quantum dot array templates can also shed light on other fundamental aspects such as quantum confinement because of the large interface between the cluster and the surrounding medium. For instance, when quantum dots are surrounded by materials having much lower refractive indices (in the optical regime) like gold, the field

[a] Technische Universität München, Heinz Maier-Leibnitz Zentrum (MLZ) Lichtenberg Strasse 1, 85748 Garching, Germany. E-mail: neelima.paul@frm2.tum.de
[b] Technische Universität München, Physik-Department, Lehrstuhl für Funktionelle Materialien, James-Franck-Str. 1, 85748 Garching, Germany
[c] Deutsches Elektronen-Synchrotron DESY, Notkestr 85, 22607 Hamburg, Germany
[d] Royal institute of Technology (KTH), Teknikringen 56-58, SE-10044 Stockholm, Sweden
[e] Technische Universität München, Physik Department, Lehrstuhl für Neutronenstreuung, James-Franck-Strasse 1, 85748 Garching, Germany. E-mail: amitesh.paul@frm2.tum.de

intensity at the interface or surface can be enhanced considerably as compared to the incident intensity. Such an enhancement in the local field is a consequence of the dielectric confinement effect and can be an important factor in describing the spectroscopy, photophysics and nonlinear optics of these clusters.[18,19] A study of the growth mechanism and morphological evolution of gold modified CdSe quantum dots can thus be useful for testing the theories of quantum confinement and obtaining particles with special spectroscopic properties.

Grazing incidence small-angle X-ray scattering (GISAXS) has proven to be a powerful tool to analyze the spatial organization and size distribution of buried particles having dimensions in the nanometer range.[20,21] Due to the increase in source brilliance at third generation synchrotron radiation sources, real-time GISAXS measurements became accessible.[22] For example, using the real-time GISAXS technique, it became possible to systematically monitor the growth behavior and corresponding morphological evolution of metal layers *in situ* during sputter deposition.[23–26] The high time resolution (milliseconds) of such real-time experiments allowed for determination of kinetics of initial nucleation as well as the subsequent clustering towards a compact layer. Typically growth laws were identified, which deepened the understanding of morphology formation.

In the present work, we expand the investigation about thin metal nanolayers formed during sputter deposition. We investigate the mechanism of gold nanostructure growth on a tailored CdSe quantum dot array to probe the templating possibilities. Real-time GISAXS experiments are used to follow the different stages of gold nanomorphology evolution during sputter deposition. This well-organized quantum dot array serves as a model template for investigating growth of gold nanostructures with *in situ* and real-time GISAXS experiments.

Experimental section

Template synthesis

The CdSe quantum dots dispersed in toluene were obtained from Bayer Technology Services, Germany. Passivating ligands like trioctylphosphine (TOP) and oleic acid (OA) were used in the synthesis to avoid agglomeration and preserve the confinement of charges. A thin layer of CdSe quantum dots was prepared on clean SiO_2 substrates by dip coating using a constant withdrawal speed of 1 mm s^{-1} under an inert atmosphere as described elsewhere in detail.[27] The resulting quantum dot array was used in the gold sputter deposition. For transmission electron microscopy (TEM) measurements, the OA and TOP capped quantum dots were prepared by dipping a polymer coated copper grid into a highly diluted suspensions of CdSe quantum dots in a manner similar to a previous study by Zillner *et al.*[28]

Transmission electron micrographs were used to determine the quantum dot size, inter-dot distances and their distributions over a local area. Measurements were done on a Philips CM12 Transmission Electron Microscope operating an accelerating voltage of 120 kV and a LaB_6 cathode. Distances between the quantum dots were determined by manually measuring the distance between their centers and calculating an average value. Similarly, quantum dot size was measured manually on several quantum dots and averaged. For the thickness measurement, the sample was scratched with a non-hardened steel needle at 2 different places and the thickness was determined at ten different positions. Using a step profiler, the average quantum dot thickness was determined to be about 7 nm.

***In situ* sputtering GISAXS** experiments were performed at the Micro- and Nanofocus X-ray scattering (MiNaXS) beamline P03 of the high brilliance light source PETRA III at DESY, Hamburg.[29] Gold was deposited by vacuum sputter deposition technique using a 99.999% gold target(from MaTecK GmbH). The sputter deposition was performed at room temperature for 600 s in Ar gas atmosphere at a pressure of 15 µbar and with an applied power of 100 W.

To calculate the final gold film thickness, gold was also grown on a bare Si substrate for 600 s. The corresponding X-ray reflectivity (XRR) data and its fit are shown in Fig. 1.

From the model used for the XRR fit, a gold film thickness of d_{Au} = 14.4 ± 1.7 nm, was extracted. Thus, the nominal sputter deposition rate was deduced to be 0.024 nm s^{-1}. Sputtering conditions were selected with a very low deposition rate to enhance the gold nanoparticle surface diffusion and prevent any premature clustering in the gaseous phase so that gold can reach the quantum dot array in its atomic state.

A PILATUS 300 K detector (DECTRIS Ltd) with a readout time of 3.6 ms and the intense photon flux enabled the *in situ* and real-time investigation of gold growth during the sputter deposition with high acquisition throughput. The detailed experimental set-up is described in detail elsewhere.[23,30] For all measurements, a wavelength of 0.09537 nm, an incident angle of 0.5° and a sample-detector distance of 2011 mm were used. A point-like beam stop was used to block the specularly reflected beam which would otherwise saturate the detector.
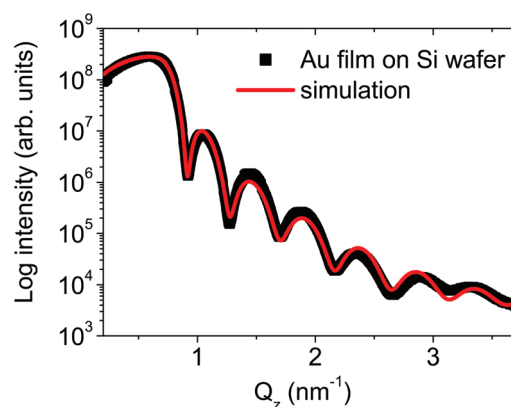

Fig. 1 X-ray reflectivity of Au covered Si substrate after 600 s deposition.

Following the scattering geometry of a typical GISAXS set-up,[31] the momentum transfer vector $\vec{Q}$ can be written as its various components:

$$Q_x = \frac{2\pi}{\lambda}\left[\cos 2\theta_f \cos \alpha_f - \cos \alpha_i\right] \quad (1)$$

$$Q_y = \frac{2\pi}{\lambda}\left[\sin 2\theta_f \cos \alpha_f\right] \quad (2)$$

$$Q_z = \frac{2\pi}{\lambda}\left[\sin \alpha_i \sin \alpha_f\right] \quad (3)$$

where α_i and α_f are incident and exit angles for scattering in the (x, z) plane, and $2\theta_f$ is the scattering angle in the (x, y) plane. The sample is located in the (x, y) plane. The Q_x element can be ignored in the case of GISAXS geometry for modelling or analysis as we do not resolve the intensities (but integrate) along that axis.

A two-dimensional intensity map is measured after the X-ray beam has been scattered from the sample. The scattered intensity is, to the 1st order, proportional to the square of the particle form factor times the interference function.[32,33] The particle form factor is the Fourier transform of the particle shape whereas the interference function is the Fourier transform of the particle–particle pair correlation function describing the particle distribution in the sample.

Modeling for treating the GISAXS data

For the analysis of the static GISAXS data modeling was done using an effective surface approximation (ESA) approach (assuming spheres as scattering objects). The statistically averaged sphere size, inter-sphere distance as well as their size and distance distribution using Gaussian functions (denoted as size/distance ± sigma distribution) were extracted. The interference function was based on a one-dimensional paracrystal model which can be described by a regular one-dimensional lattice having a cumulative loss of long range order.[34] In the applied modeling of the intensity of the one-dimensional horizontal line cuts (along Q_y at a particular Q_z position the contribution from the spheres along the Q_z direction (corresponding to the height of the spheres) was neglected.[31] For very low Q_y values, the experimental resolution limit of the instrument was taken into account and modeled using a Lorentzian-shaped function. IsGISAXS was used for simulation of the measured two-dimensional (2D) GISAXS patterns.[32]

For the analysis of the time-resolved GISAXS data, one-dimensional line cuts were taken using the full time resolution to extract information on the kinetics of gold growth. The ESA was used again for fitting the horizontal line cuts with Lorentzian distribution functions.[35] Diffuse scattering with GISAXS includes a Q_y resolution which increases the complexity of experimental interpretation. Thus, approaches like ESA are used for simplification of the scattering cross-section within the distorted wave born approximation (DWBA). The differential cross-section includes the diffuse scattering intensity which is dominated by the Fourier transform of the height–height correlation function of only one effective surface hence 'ESA'.[36] In this way, the diffuse scattering factor is approximated to depend on the form factor of the individual objects and also on the structure factor. The temporal evolution of the peak position and peak width enabled us to track the relevant structural changes occurring in the gold thin film during sputter deposition.[23,37]

Results and discussion

Quantum dot array: before and after gold nanostructure growth

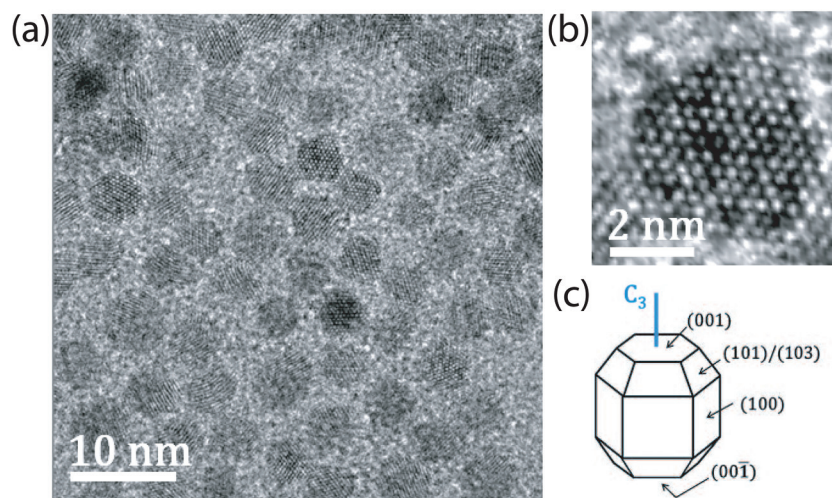Fig. 2(a) shows a transmission electron micrograph of the CdSe quantum dot array and Fig. 2(b) presents a magnified

Fig. 2 (a) TEM image of CdSe quantum dot array, (b) enlarged TEM view of a single CdSe quantum dot oriented along the (001) axis, (c) wireframe outline of a model crystallite. This image has been reproduced from ref. 38 with permission.

TEM view of a single CdSe quantum dot. The typical wireframe outline of a model quantum dot is depicted in Fig. 2(c). The diameter of a single quantum dot as measured from the TEM images is 4.5 ± 0.5 nm. The quantum dot array shows a well-defined distribution of the quantum dots with a distance of 7.7 ± 0.2 nm between centers of the neighboring quantum dots. The CdSe crystallites within the quantum dot (in Fig. 2(b)) show atomic columns with hexagonal arrangement indicating an [0001] orientation of the CdSe dot (the inter-atomic distance being equal to the lattice parameter 'a' of the wurtzite structure). Such a regular hexagonal arrangement of CdSe quantum dots has also been observed during another study on shape control of CdSe nanocrystals.[39] Recently, well-

organized hexagonal ordering of similar dimensions has also been reported for PbSe quantum dots.[40]

Complementary to TEM, which measures the local morphology of a very small part of the quantum dot array, GISAXS probes the large scale morphology with a high statistical relevance. GISAXS is performed to investigate if the observed surface morphology extends over the entire array and within the inner film volume. Thus, GISAXS measurements can deliver statistically averaged values for the quantum dot radius and inter-dot distance, which are representative of the whole array.

Fig. 3(a) shows the two-dimensional GISAXS data of the bare quantum dot array where some pronounced features such
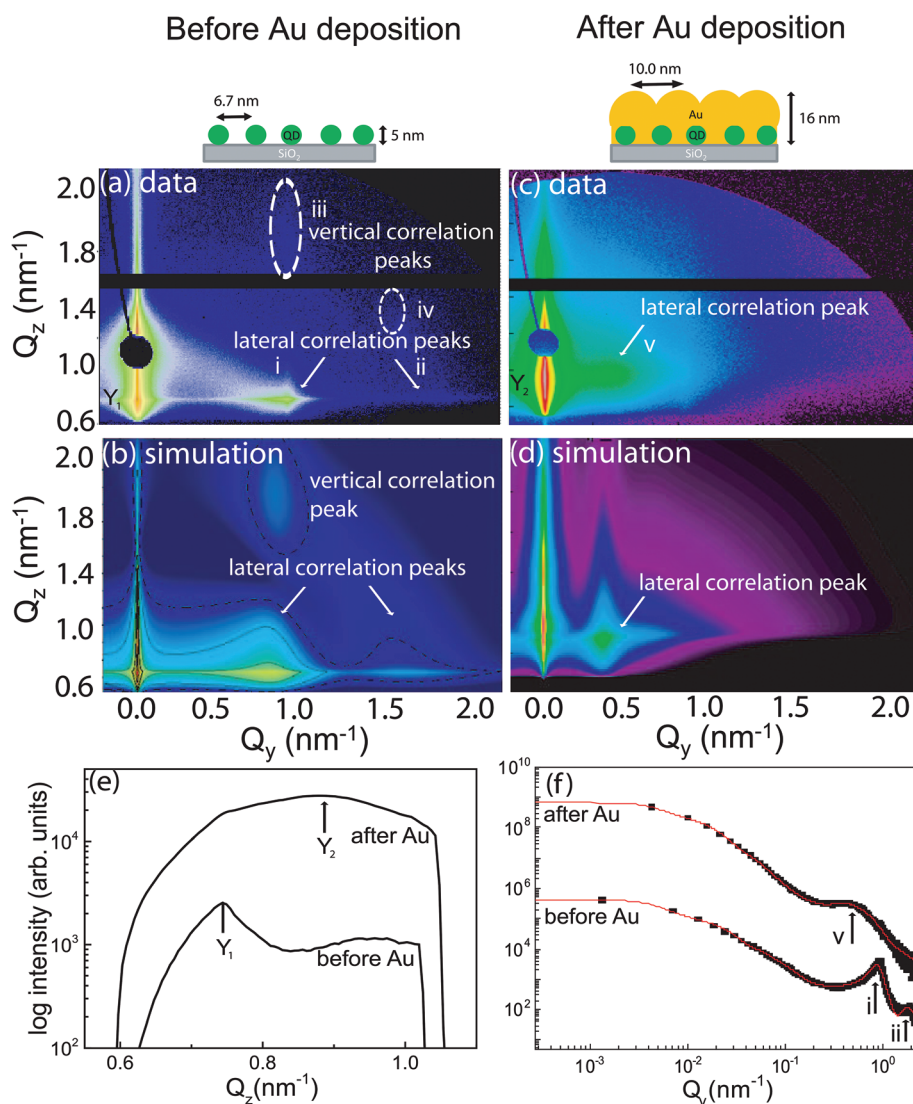

Fig. 3 Two-dimensional GISAXS data of the quantum dot array (a) before and (c) after gold deposition are shown along with simulated GISAXS patterns (b) before and (d) after gold deposition. Characteristic structures are highlighted and explained in the text. (e) One-dimensional vertical line cuts along $Q_y = 0$ nm^{-1} before (bottom curve) and after (top curve) gold deposition are shown with highlighted Yoneda peak positions Y_1 and Y_2. (f) One-dimensional horizontal line cuts (solid black rectangles) across the Yoneda maximum before (bottom curve) and after (top curve) gold deposition are shown together with their fits (red lines) using a model as described in the text. At the top, a schematic shows the side-view morphology of the quantum dot array before and after gold deposition.
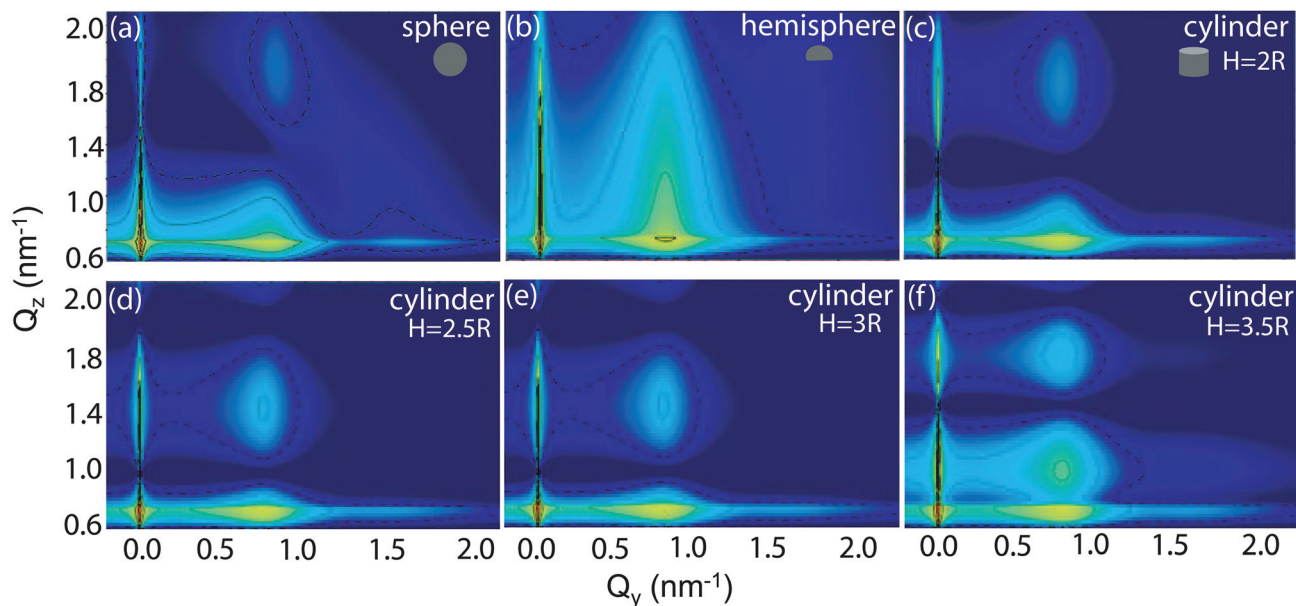
Fig. 4 IsGISAXS simulations of the bare quantum dot template for a fixed dot radius $R = 2.5$ nm and various shapes and heights such as (a) sphere, (b) hemisphere, (c) cylinder $H = 2R$, (d) cylinder $H = 2.5R$, (e) cylinder $H = 3R$ and (f) cylinder $H = 3.5R$.

as Yoneda peak, peaks due to lateral and vertical correlations are highlighted. The circular black shielding is due to the Pb beam stop which is mounted to prevent detector saturation from the intense specular beam. The horizontal black line is the inter-module gap of the Pilatus detector. The material characteristic Yoneda peak (Y_1), causing a maximum in the scattered intensity, is located below the specular peak at $Q_y = 0$ nm^{-1}. One very intense peak due to a lateral correlation (or the 1st order lateral correlation peak), indicated by a white arrow (i), is visible at $Q_y = 0.92$ nm^{-1} at $Q_z = 0.75$ nm^{-1}. It arises from the in-plane nearest-neighbor short-range ordering of the CdSe quantum dots. A faint 1st order scattering maximum (or the vertical correlation peak), indicated by the dashed white ellipse (iii), can be noticed directly above this peak due to a vertical correlation in the dots. This is usually an indication of a nearly uniform height of the quantum dots with only small variances.[25] Another weaker lateral correlation peak (2nd order) seen at $Q_y = 1.8$ nm^{-1} and indicated by a white arrow (ii), shows the extension of the short range ordering to the next-nearest-neighbor level. For this lateral correlation peak as well, a faint 2nd order scattering maximum (iv) in the vertical direction (but at a lower $Q_y = 1.62$ nm^{-1}) value can be seen.

Three distinct features (a) appearance of the 2nd order vertical correlation peak (iv) at a lower Q_y value (as compared to the Q_y position of the 2nd order lateral correlation peak (ii)), (b) the relative weak intensity of this height modulation and (c) a faint ring like halo are indications of a spherical shape of the quantum dots. A further inference on the shape of the quantum dots can be drawn by simulating the full two-dimensional intensity map using the IsGISAXS software. We considered various shape geometries such as spheres, hemispheres and cylinders with different aspect ratios in our

modelling as can be seen in Fig. 4. The most reasonable agreement between the experimental data and the simulated two-dimensional GISAXS pattern is observed for a spheroidal shape geometry (Fig. 4(a)) which is shown also in Fig. 3(b). The main features of the two-dimensional GISAXS data such as the positions of the peaks due to the lateral correlation in Q_y and the positions of the vertical correlation peaks in Q_z at two different Q_y positions are well reproduced in the simulation. The estimated height of the quantum dot from this model is around 5 nm.

A one-dimensional vertical line cut of the two-dimensional GISAXS data along Q_z is shown in Fig. 3(e). The Yoneda maximum (Y_1) is located at a Q_z value of 0.75 nm^{-1} corresponding to an experimental scattering length density (SLD) value of 2.22×10^{-5} Å^{-2}. This SLD value is similar to the theoretical SLD value of SiO$_2$(2.27×10^{-5} Å^{-2}), which is the substrate for the quantum dot array. A one-dimensional horizontal line cut along Q_y of the two-dimensional GISAXS data is shown in Fig. 3(f). The data is fitted with a model similar to that used in the IsGISAXS simulation. The most prominent size distribution extracted from this model corresponds to an average quantum dot diameter of 5.2 ± 0.2 nm and an average inter-dot spacing of 6.7 ± 0.3 nm. These values are in good agreement with those obtained from the TEM measurements.

After completion of the gold deposition, the sample is again investigated with GISAXS. The two-dimensional GISAXS data of the quantum dot array after gold deposition is shown in Fig. 3(c). As compared to the GISAXS data of the bare quantum dot array, the 1st order lateral correlation peak has shifted to a lower Q_y position, indicated by a white arrow (v). This shift is attributed to the formation of a new surface morphology during the gold deposition. An enhancement of the
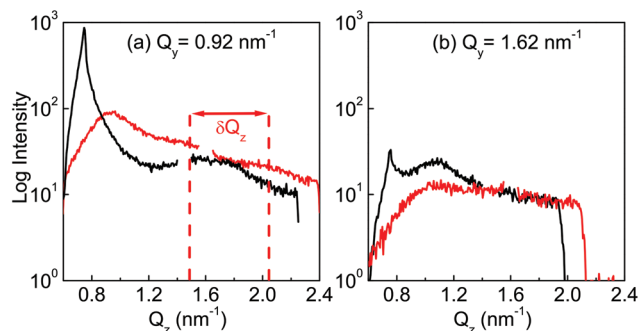
Fig. 5 One-dimensional vertical line cuts for the entire Q_z range for (a) 1st order vertical correlation peak (iii) located at $Q_y = 0.92$ nm^{-1} and (b) 2nd order vertical correlation peak (iv) located at $Q_y = 1.62$ nm^{-1}, before (black) and after (red) gold deposition on the quantum dot array. Due to the higher scattering length density of the CdSe–gold layer, the maximal Q_z position has shifted (along with the Yoneda maximum) from 0.75 nm^{-1} to 0.94 nm^{-1} after gold deposition.

scattering intensity below the circular beam stop (noticeable also in Fig. 3(e)) is due to presence of an additional Yoneda peak (Y$_2$) of gold–CdSe being located at a higher Q_z value. Above the circular beam stop, the intensity increases due to

the Kiessig oscillation, which originate from the finite thickness of the thin gold film on the quantum dot array.

Based on IsGISAXS, the simulated two-dimensional GISAXS pattern for the quantum dot array after gold deposition is shown in Fig. 3(d). The model assumes a mixed gold–CdSe (50 : 50) layer of 5 nm thickness having a high roughness with 11 nm thick gold hemispherical clusters on top. The main feature of the two-dimensional GISAXS data such as the lateral correlation peak (v) position in Q_y is again well reproduced in the simulation. The estimated height of the gold capped quantum dot array from this model is 16 nm. The one-dimensional horizontal line cut is fitted with the model similar to that used in the IsGISAXS simulation. The most prominent size distribution extracted from this model corresponds to an average particle diameter of 5.4 ± 0.3 nm and an average interparticle spacing of 10.0 ± 1.2 nm. The scattering signal from the initial long range distribution of the quantum dot arrangement is now dominated by the signal from the arrangement of the gold clusters, which does not replicate the morphology of the initial regular quantum dot arrangement. Moreover, the initially observed 2nd order peak due to the lateral correlation has disappeared. This demonstrates a loss in the long range order of the newly formed structure.
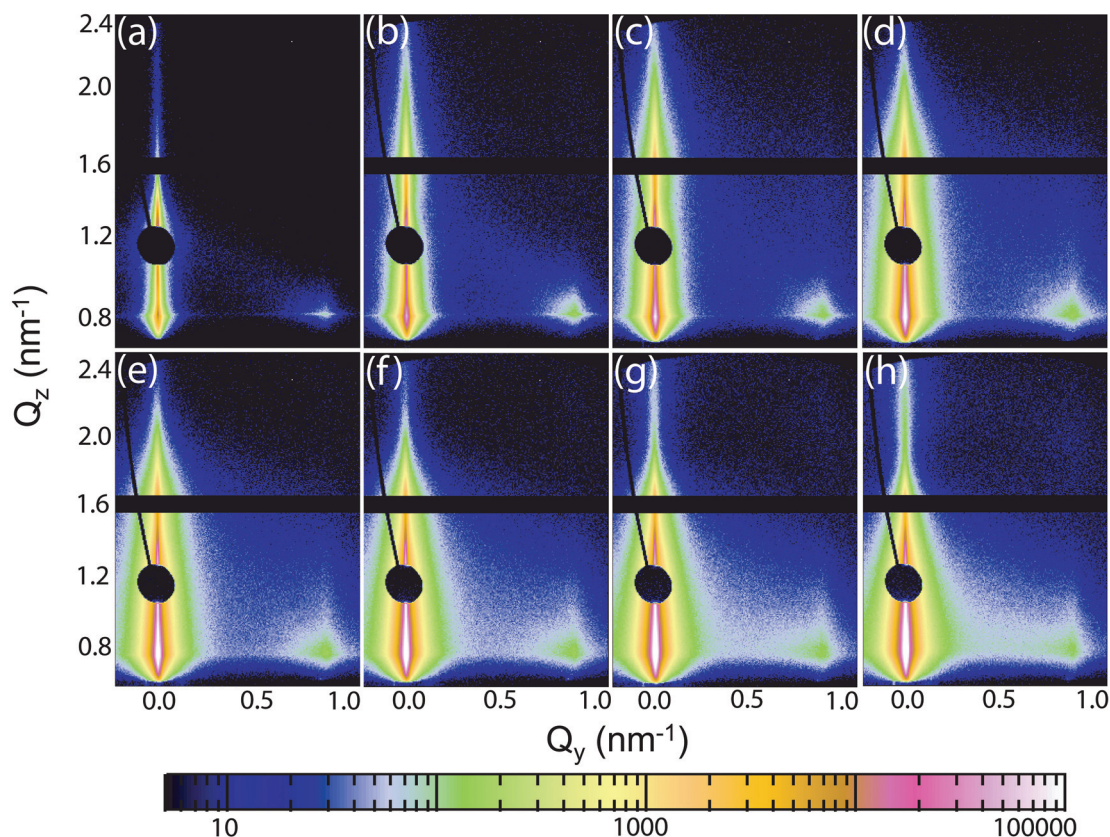

Fig. 6 Selected two-dimensional GISAXS data from the *in situ* gold sputter deposition on the quantum dot array showing the early stages. Data are taken (a) before and during deposition for different gold thicknesses d_{Au}: (b) 0.48 nm, (c) 0.96 nm, (d) 1.68 nm, (e) 2.16 nm, (f) 2.64 nm, (g) 3.12 nm and (h) 3.60 nm.

One-dimensional vertical cuts at $Q_y = 0.92$ nm^{-1} and $Q_y = 1.62$ nm^{-1}, corresponding to the first and second order vertical correlation peaks, both before and after gold deposition, are shown in Fig. 5. From the distance between the two adjacent vertical maxima (ΔQ_z), an average thickness of the Au layer on top of the quantum dot layer was extracted as 11.5 ± 0.4 nm using the simple approach based on eqn (4):

$$d = \frac{2\pi}{\Delta Q_z} \quad (4)$$

This thickness value differs from that extracted from the XRR measurement of gold on bare Si substrate (14.4 ± 1.7 nm). However, it may be noted that only with XRR the film thickness is probed directly along the Q_z direction ($\perp^r$ to the film-plane), whereas the vertical line cuts along Q_z in GISAXS measurements have an offset with the axes $\perp^r$ to the sample plane. Thus, the intensity modulations along Q_z are not the same for the XRR and GISAXS geometries. Moreover, gold growth on bare Si might differ in thickness from that on the quantum dot template.

Intermediate morphologies during gold sputtering

In order to understand how the initial quantum dot array is coated with gold in terms of the morphological evolution, a detailed *in situ* study is required. With time-resolved GISAXS, it is possible to follow the evolution of characteristic structures *in situ* during the gold sputter deposition.

Two-dimensional GISAXS data are recorded during the gold deposition with a high time resolution to obtain full information about the gold growth on the quantum dot array. This template consists of two different materials, namely semiconductor CdSe quantum dots on an insulator SiO$_2$ matrix. As a consequence, it is interesting to investigate if the gold atoms have a preference for either of these two chemically different regions as nucleation sites for deposition. The observed growth process is spilt into two sections to separate the early stage of the dominating in-plane (horizontal) growth from the vertical growth at later stages.

Nucleation and lateral growth of gold. Fig. 6 shows eight selected two-dimensional GISAXS data of the gold sputter deposition on the quantum dot array covering a range from 0 s to 150 s deposition time. The shown data correspond to gold films with thicknesses $d_{Au} = 0$ nm, 0.48 nm, 0.96 nm, 1.68 nm, 2.16 nm, 2.64 nm, 3.12 nm and 3.60 nm. With an increasing gold film thickness, the intensity of the 1st order lateral correlation peak at $Q_y = 0.92$ nm^{-1} is enhanced along the Q_y as well as along the Q_z axis. In Fig. 7(a), changes in width of the 1st order lateral correlation peak (located at $Q_y = 0.92$ nm^{-1}) along the Q_y as well as along the Q_z axes, are plotted as a function of d_{Au}. In the inset, the peak positions of the 1st and 2nd order lateral correlation in Q_y are shown as a function of d_{Au}. The position of the 1st order lateral correlation peak remains fairly constant even at $d_{Au} = 3.6$ nm whereas the peak position of the 2nd order peak could not be traced anymore after $d_{Au} = 0.48$ nm. This implies that the gold deposition is inducing a change from a regular spatial arrangement to a more

disordered arrangement (plausibly due to the presence of small diffusing gold clusters) after the thickness reached $d_{Au} \approx 0.48$ nm. This indicates the formation of a different gold–gold inter-particle distance.

The increase in the FWHM along Q_z (black curve) indicates that there is a decrease in the vertical correlation length with increasing d_{Au}. One can also observe a significant change in slope around $d_{Au} = 0.48$ nm. A steeper slope is indicative of a stronger vertical correlation, typical of a growth maintaining the preferred nucleation sites. Above $d_{Au} = 0.48$ nm, the initial preferred nucleation sites for the gold deposits (on top of the quantum dots) are gradually lost with the loss in the corresponding vertical correlation.

From Fig. 7(a), one can observe that the FWHM along Q_y (red curve) of the 1st order peak remains constant only below an initial thickness, d_{Au} of 0.48 nm. Above $d_{Au} = 0.48$ nm, the FWHM of the peak shows an abrupt jump. This broadening indicates an increase in the distribution of size and inter-particle spacing. This can be visualized as due to gold nanoparticles positioning around the dots (and not only
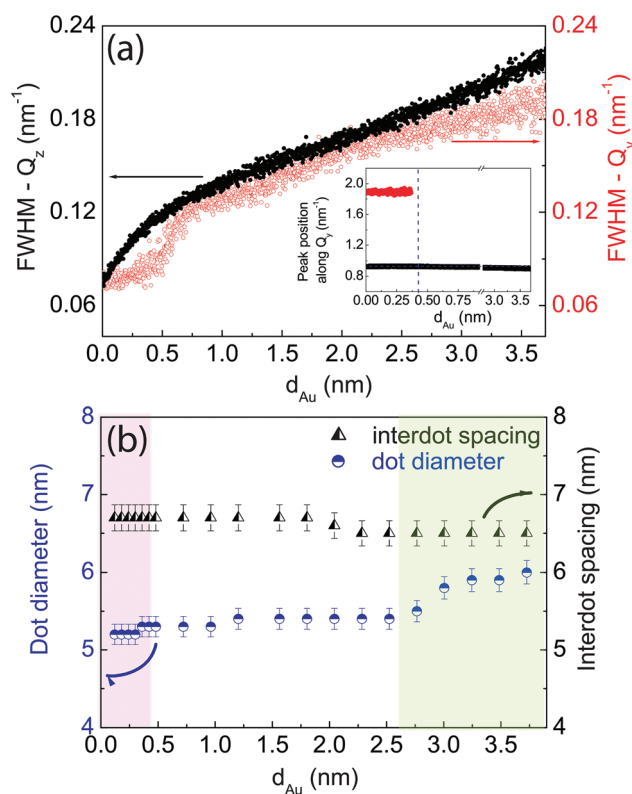

Fig. 7 (a) Evolution of the peak broadening or full width at half maximum (FWHM) of the 1st order lateral correlation peak (i) as function of thickness d_{Au}, along Q_y (red open circles) as well as along Q_z (black closed circles). Inset (a) Evolution of the 1st order lateral correlation (black closed circles) and 2nd order (red closed circles) lateral correlation peak positions with d_{Au}. Note that the 2nd order peak due to lateral correlation disappears after $d_{Au} = 0.48$ nm is reached. (b) Evolution of dot diameter and inter-dot spacing as function of d_{Au}.

on the dots) and thereby increasing the effective size of the dots.

This trend can also be confirmed from the plot in Fig. 7(b), which shows the variation of the quantum dot size and the inter-dot spacing as a function of d_{Au}. Below a thickness of about $d_{Au} = 0.48$ nm both parameters remain fairly constant, which implies that the gold deposition is undergoing a change, which can be related purely to the height and not to lateral structures. An initial preferential accumulation of gold on top of the quantum dots is observed or in other words, gold nanoparticles perfectly decorate the quantum dots, maintaining the template structure. Above $d_{Au} = 0.48$ nm no significant change in the dot diameter or the inter-dot spacing is seen up to $d_{Au} \approx 2.5$ nm. Thus, the increasing height does not affect the growth morphology in this regime. Above $d_{Au} \approx 2.5$ nm the dot diameter increases and the inter-dot distance decreases. These changes in both parameters signify the diffusion of gold–gold clusters – creating a cluster morphology different from the initial quantum-dot template.

Thus, initially there is an accumulation of gold atoms at and around the quantum dots (which act as preferred nucleation sites), followed by their lateral growth leading to a gradual coalescence and a systematic formation of a mixed gold-dot compact layer. The scattering length density (SLD) of Au is 12.46×10^{-5} Å^{-2}, which is higher than the SLD value of CdSe (4.2×10^{-5} Å^{-2}). As a consequence, with the successive accumulation of gold, an increase in the diffuse scattering from the sample surface is expected and is seen around $Q_y = 0$ nm^{-1}. Decoration of dots observed in the present work is in contrast to previous investigations, where in the GISAXS data, a peak due to lateral correlation constantly moves from far Q_y values towards low values during metal deposition on either bare Si surface or on polymer films.[23,41] In those studies, a random nucleation of gold nanoparticles on the solid surfaces was followed by lateral gold cluster growth, which initially had a smaller in-plane correlation length, but as growth proceeded and coalescence occurred, the in-plane correlation length increased and accordingly gold cluster related peak due to lateral correlations moved towards lower Q_y values. In contrast, in the present study after the formation of mixed gold-dot particles, a characteristic scattering peak for a gold structure deviating from that of the quantum dots can not be traced.

Vertical growth of gold. Fig. 8 shows eight selected GISAXS data measured during gold sputter deposition on the quantum dot array in a deposition time span from 200 s to 650 s. The corresponding thickness d_{Au} are 4.8 nm, 6.0 nm, 7.2 nm,
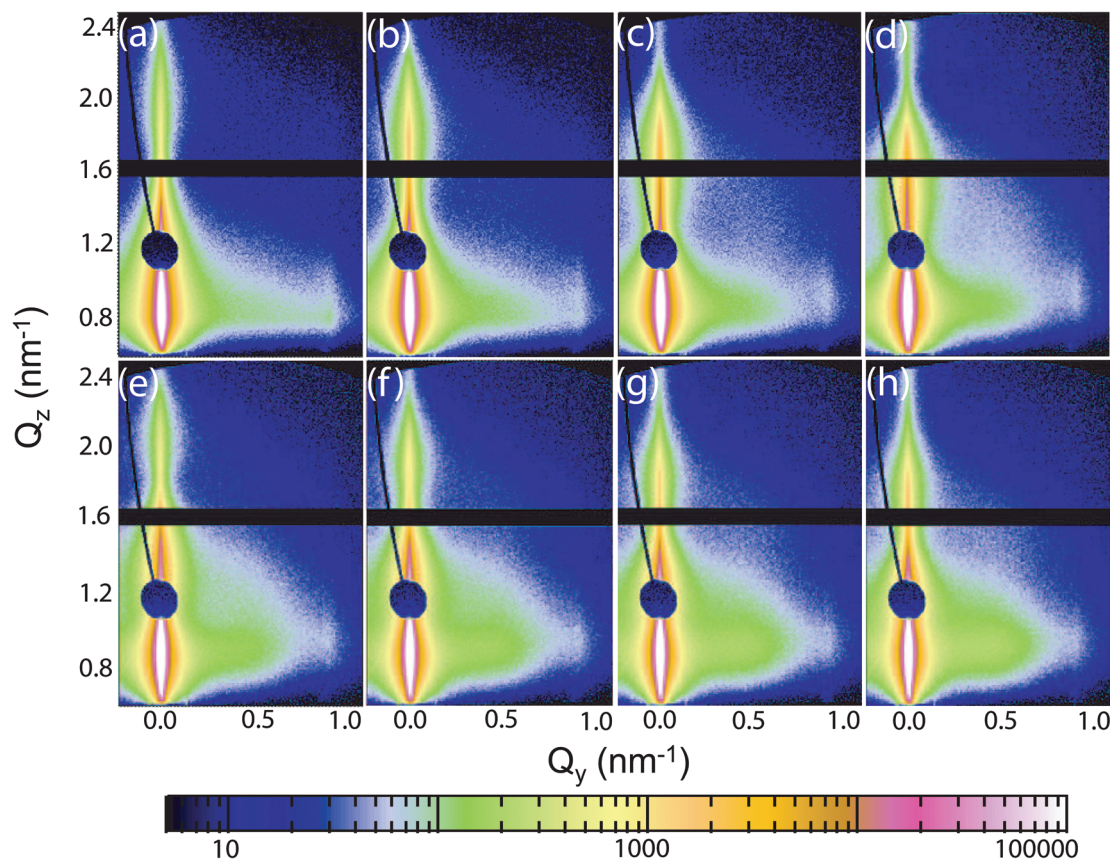

Fig. 8 Selected two-dimensional GISAXS data from the *in situ* gold sputter deposition on the quantum dot array showing the late stages of growth. Data are taken during deposition for different thicknesses, d_{Au}: (a) 4.8 nm, (b) 6.0 nm, (c) 7.2 nm, (d) 8.4 nm, (e) 10.8 nm, (f) 12.0 nm, (g) 13.2 nm and (h) 14.4 nm.

8.4 nm, 10.8 nm, 12.0 nm, 13.2 nm, 14.4 nm, respectively. These data show several prominent features evolving during the persisting gold deposition. The intensity along the Q_z direction is seen to change periodically in a oscillatory manner showing the changes in the periodicity of the total thickness oscillations (Kiessig oscillations) of the deposited gold film with time. These changes indicate an increase in thickness. In addition, with time, the intensity of the characteristic peak due to lateral correlation due to the quantum dot array gradually decreases. At this stage, the growth proceeds mainly via vertical growth of the gold film.

In Fig. 9, selected one-dimensional vertical and horizontal line cuts are shown from the real-time study. For the X-ray wavelength used in the present experiment the critical angles of SiO₂, CdSe and gold are 0.146°, 0.199°and 0.343°, respectively. These correspond to Q_z values of 0.75 nm⁻¹, 0.81 nm⁻¹ and 0.97 nm⁻¹, respectively according to the eqn (3), As mentioned earlier, the Yoneda peak for the quantum dot array on SiO₂ corresponds to an experimental SLD value of 2.22×10^{-5} Å⁻². The second Yoneda peak which emerges after 200 s (see Fig. 9(a)) can be attributed to a mixed CdSe–gold layer having an experimental SLD value of 8.3×10^{-5} Å⁻², which is exactly the average of the theoretical SLDs of CdSe (4.2×10^{-5} Å⁻²) and gold (12.4×10^{-5} Å⁻²) compact layers assuming a 50 : 50 composition. In Fig. 9(b), one observes thickness oscillations which appear at high Q_z values and move towards lower Q_z values with time (and d_{Au}). In Fig. 9(c), one sees at an initial stage the prominent 1ˢᵗ order peak due to lateral correlation (dashed arrow I) from CdSe quantum dots. After d_{Au} of 4.8 nm, another peak due to lateral correlation (dashed arrow II) starts to emerge and gradually moves to slightly lower Q_z values with time.

In Fig. 10, mappings extracted from the two-dimensional GISAXS data are shown to clarify the evolving structures. An overview of the temporal evolution of vertical and horizontal structures is gained from these maps. Fig. 10(a) and (b) show the time evolution of the vertical cuts taken at constant $Q_y = 0.92$ nm⁻¹ and at constant $Q_y = 0$ nm⁻¹, respectively. They exhibit temporal evolution of the structures perpendicular to the sample surface, which translates into its evolution with d_{Au}. The thickness oscillations shown in Fig. 9(b) give rise to the oscillating intensity waves with varying Q_z in Fig. 10(a) and (b).

Fig. 10(c) represents the time evolution of the horizontal line cuts taken at the Yoneda peak with the full time resolution of the real-time experiment. In general, horizontal line cuts are sensitive to structural features parallel to a quantum dot array. Thus, Fig. 10(c) represent the temporal lateral structure evolution which translates into changes with increasing thickness d_{Au}. The peak due to lateral correlation or intensity maxima at $Q_y = 0.92$ nm⁻¹, is very intense in the initial stages till $d_{Au} \approx$ 3.6 nm, due to short range ordering of CdSe quantum dots. For larger d_{Au}, its intensity gradually decreases and the scattering is dominated by the scattering from the compact gold layer which has formed on the template by this time. Subsequent deposition leads to nanoparticle cluster growth and coalesc-
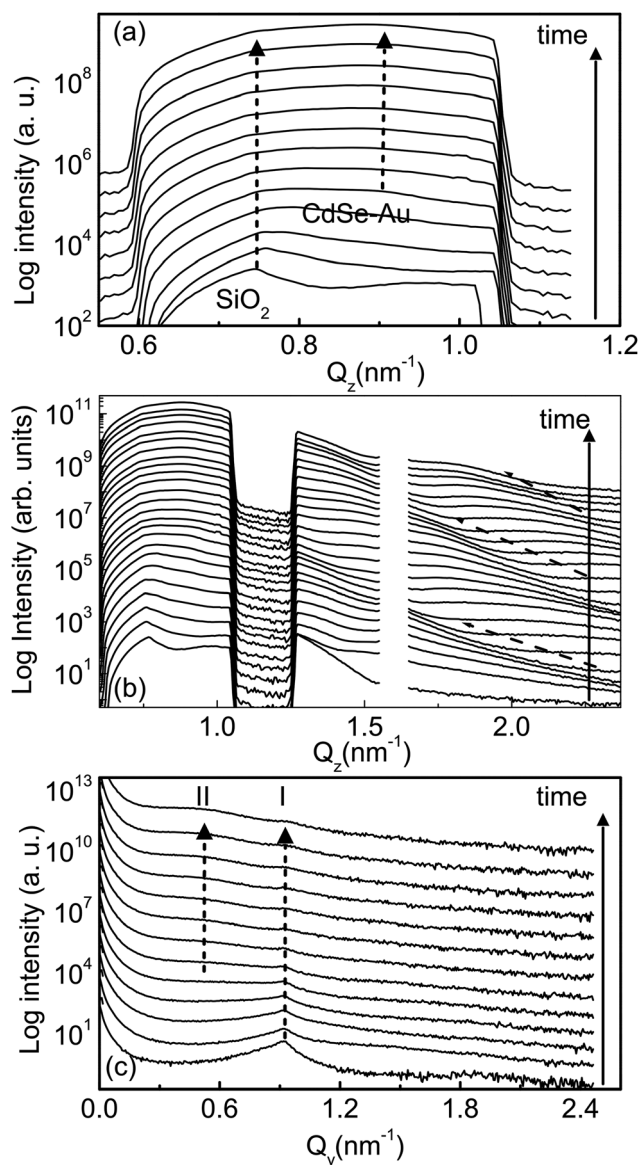

Fig. 9 (a) One-dimensional vertical line cuts at $Q_y = 0$ nm⁻¹ for a selected Q_z range (b) one-dimensional vertical line cuts at $Q_y = 0$ nm⁻¹ for the full Q_z range and (c) one-dimensional horizontal line cuts at a constant $Q_z = 0.75$ nm⁻¹ for different thicknesses d_{Au}: From bottom to top 0 nm, 1.2 nm, 2.4 nm, 3.6 nm, 4.8 nm, 6.0 nm, 7.2 nm, 8.4 nm, 9.6 nm, 10.8 nm, 12.0 nm, 13.2 nm and 14.4 nm. The arrows I and II indicate the characteristic lateral correlation peaks of the quantum dots and the gold nanostructures respectively.

ence in agreement with the behavior observed in studies on other systems.[23,25,41]

Growth model

The morphologic evolution of gold nanostructure growth on the quantum dot array is schematically depicted in Fig. 11. The regular arrangement of the quantum dots in the template causes peak due to lateral correlations (denoted with 'i' and 'ii' in Fig. 3(a)). In the early stages of growth, gold decorates pre-
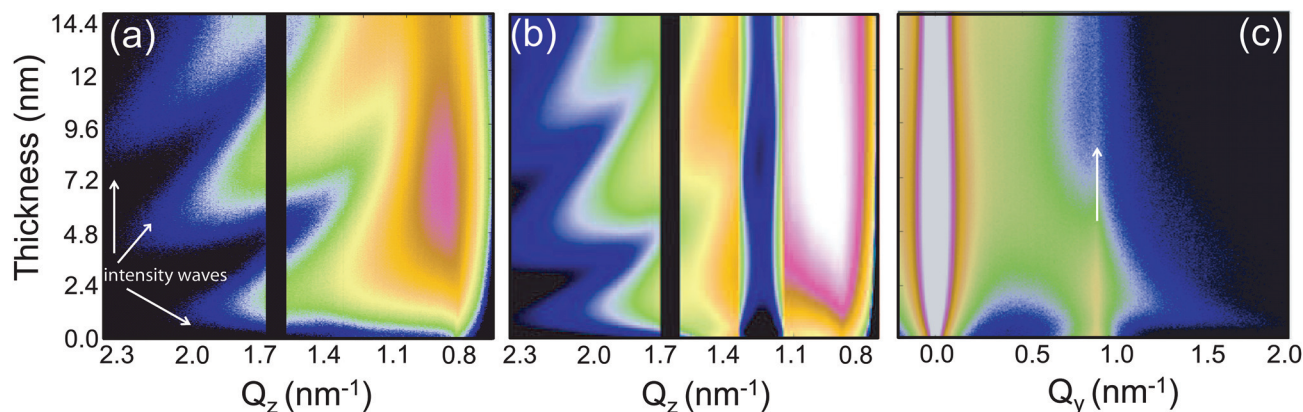
Fig. 10 Mapping of vertical line cuts from the time-resolved two-dimensional GISAXS data taken at (a) $Q_y = 0.92$ nm^{-1} and at (b) $Q_y = 0$. (c) Mapping of horizontal line cuts from the time-resolved two-dimensional GISAXS data taken at the Yoneda maximum position. The solid white arrow follows the Au growth at quantum dots characteristic peak due to lateral correlation position.
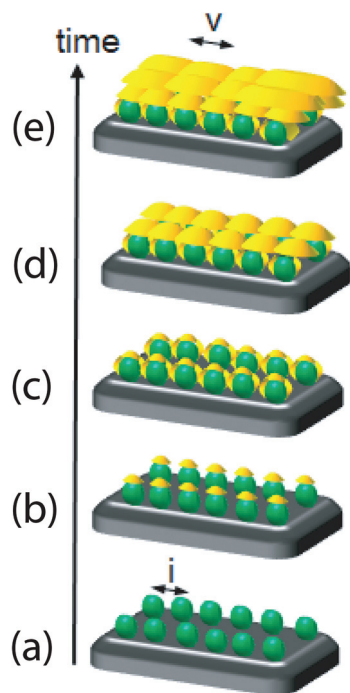

Fig. 11 Schematic drawing of gold nanostructure growth on the quantum dot array: (a) Bare quantum dot array where a regular inter-particle distance causes the peak due to lateral correlation 'i' (and 'ii') in Fig. 3(a). (b) Directed nucleation of gold on top of the quantum dots. (c) Lateral growth of gold nanostructures to form a CdSe−gold layer. (d) and (e) Its subsequent vertical and lateral growth. A comparatively less regular inter-particle distance causes the peak due to lateral correlation 'v' in Fig. 3(c).

ferentially the top of the quantum dots. Therefore, in this early stage of growth the quantum dot array has a strong templating effect on the deposited gold. This early stage is followed by lateral gold growth around the quantum dots to form a mixed gold–CdSe layer. The evolved mixed gold-dot particles gets irre-

gular in shape so that center-to-center distances become less uniform compared those of the gold-free surface, leading to a less ordered correlation. After formation of a complete layer, gold growth proceeds predominantly in the vertical direction. However, it is also accompanied by grain growth leading to larger in-plane length scales as compared with the original quantum dot array. The final in-plane arrangement is comparatively less ordered than the quantum dot template and causes a peak due to lateral correlation (denoted with 'v' in Fig. 3(c)). Thus, at this stage of growth the templating effect of the quantum dot surface is lost.

Conclusion

The growth of gold nanostructures on a CdSe quantum dot array is probed using time-resolved GISAXS. The growth process is followed from nucleation on top of the quantum dots to the formation of a continuous gold-dot mixed layer and finally to a gold capping layer, which has a morphology decoupled from that of the quantum dot array. Morphological parameters, such as radii and correlation distance, for the bare quantum dots and for the evolving gold-dot clusters are extracted by modeling the GISAXS data. In the initial stages of gold deposition, the gold atoms selectively accumulate on quantum dots (which act as nucleation sites). The high mobility of the gold atoms and its selective interaction with the quantum dots causes this preferential accumulation of gold on top of the quantum dots. After having reached a thickness $d_{Au} \approx 0.48$ nm, growth proceeds by lateral growth and coalescence of these gold-dot clusters to form a compact gold-dot layer. Above $d_{Au} = 3.6$ nm, the gold growth proceeds mainly in the vertical direction, meaning along the surface normal of the substrate to form a gold capping layer. However, some lateral growth via outward shift of cluster boundaries still continues.

As a consequence, we have worked out a condition to have gold metal nanocontacts positioned directly on top of

quantum dots only. For such local contact formation in the nanoscale, a clever combination of a low deposition rate and a gold film thickness less than $d_{Au} \approx 0.48$ nm is required. These structures will be of interest for the next generation quantum dots based nanoelectronic devices serving as stable metal contacts for local charge transfer or for interconnecting the dot array.

Acknowledgements

References

1 A. P. Alivisatos, *Science*, 1996, **271**, 933–937.
2 P. R. Brown, D. Kim, R. R. Lunt, N. Zhao, M. G. Bawendi, J. C. Grossman and V. Bulovi, *ACS Nano*, 2014, **8**, 5863–5872.
3 A. G. Pattantyus-Abraham, I. J. Kramer, A. R. Barkhouse, X. Wang, G. Konstantatos, R. Debnath, L. Levina, I. Raabe, M. K. Nazeeruddin and M. Grätzel, *ACS Nano*, 2010, **4**, 3374–3380.
4 A. Kongkanand, K. Tvrdy, K. Takechi, M. Kuno and P. V. Kamat, *J. Am. Chem. Soc.*, 2008, **130**(12), 4007–4015.
5 H. Lee, M. Wang, P. Chen, D. R. Gamelin, S. M. Zakeeruddin, M. Grätzel and M. K. Nazeeruddin, *Nano Lett.*, 2009, **9**, 4221–4227.
6 P. V. Kamat, *J. Phys. Chem. C*, 2008, **112**(48), 18737–18753.
7 T. Schmidt, T. Clausen, J. Falta, S. Bernstorff, G. Alexe, T. Passow and D. Hommel, *Phys. Status Solidi B*, 2004, **241**, 523–526.
8 T. Schmidt, E. Roventa, G. Alexe, T. Clausen, J. I. Flege, S. Bernstorff, A. Rosenauer, D. Hommel and J. Falta, *Appl. Phys. Lett.*, 2004, **84**, 4367–4369.
9 J. S. Foresi and T. D. Moustakas, *Appl. Phys. Lett.*, 1993, **62**, 2859–2861.
10 L. Etgar, *Materials*, 2013, **6**, 445–459.
11 R. J. Matson, O. Jamjoum, A. D. Buonaquisti, P. Russell, L. L. Kazmerski, P. Sheldon and R. K. Ahrenkiel, *Solar Cells*, 1984, **11**, 301–305.
12 A. Yakimov and S. R. Forrest, *Appl. Phys. Lett.*, 2002, **80**, 1667–1669.
13 H. Hadipour, B. de Boer and P. W. M. Blom, *Adv. Funct. Mater.*, 2008, **18**, 169–181.
14 X. Wu, X. He, K. Wang, C. Xie, B. Zhou and Z. Qing, *Nanoscale*, 2010, **2**, 2244.
15 J. Zheng, C. Zhou, M. Yu and J. Liu, *Nanoscale*, 2012, **4**, 4073–4083.
16 Y. Yeh, B. Creran and V. Rotello, *Nanoscale*, 2012, **4**, 1871–1880.
17 R. Jin, *Nanoscale*, 2010, **2**, 343–362.

18 Y. Wang and N. Herron, *J. Phys. Chem.*, 1991, **95**, 525–532.
19 G. Santoro, S. Yu, M. Schwartzkopf, P. Zhang, S. K. Vayalil, J. F. H. Risch, M. A. Rübhausen, M. Hernandez, C. Domingo and S. V. Roth, *Appl. Phys. Lett.*, 2014, **104**, 243107.
20 G. Renaud, R. Lazzari and F. Leroy, *Surf. Sci. Rep.*, 2009, **64**, 255–380.
21 D. Babonneau, S. Camelio, E. Vandenhecke, S. Rousselet, M. Garel, F. Pailloux and P. Boesecke, *Phys. Rev. B: Condens. Matter*, 2012, **85**, 235415.
22 C. J. Schaffer, C. M. Palumbiny, M. A. Niedermeier, C. Jendrzejewski, G. Santoro, S. V. Roth and P. Müller-Buschbaum, *Adv. Mater.*, 2013, **25**, 6760–6764.
23 M. Schwartzkopf, A. Buffet, V. Körstgens, E. Metwalli, K. Schlage, G. Benecke, J. Perlich, M. Rawolle, A. Rothkirch, B. Heidmann, G. Herzog, P. Müller-Buschbaum, R. Röhlsberger, R. Gehrke, N. Stribeck and S. V. Roth, *Nanoscale*, 2013, **5**, 5053–5062.
24 S. Yu, G. Santoro, K. Sarkar, B. Dicke, P. Wessels, S. Bommel, R. Döhrmann, J. Perlich, M. Kuhlmann, E. Metwalli, J. F. H. Risch, M. Schwartzkopf, M. Drescher, P. Müller-Buschbaum and S. V. Roth, *J. Phys. Chem. Lett.*, 2013, **4**, 3170.
25 G. Kaune, M. A. Ruderer, E. Metwalli, W. Wang, S. Couet, K. Schlage, R. Röhlsberger, S. V. Roth and P. Müller-Buschbaum, *ACS Appl. Mater. Interfaces*, 2009, **1**(2), 353–360.
26 E. Metwalli, S. Couet, K. Schlage, R. Röhlsberger, V. Korstgens, M. Ruderer, W. Wang, G. Kaune, S. V. Roth and P. Müller-Buschbaum, *Langmuir*, 2008, **24**, 4265–4272.
27 E. Zillner and T. Dittrich, *Phys. Status Solidi RRL*, 2011, **5**, 256–258.
28 E. Zillner, S. Fengler, P. Niyamakom, F. Rauscher, K. Kohler and T. Dittrich, *J. Phys. Chem. C*, 2012, **116**, 16747–16754.
29 A. Buffet, A. Rothkirch, R. Döhrmann, V. Körstgens, M. M. Abul Kashem, J. Perlich, G. Herzog, M. Schwartzkopf, R. Gehrke, P. Müller-Buschbaum and S. V. Roth, *J. Synchrotron Radiat.*, 2012, **19**, 647–653.
30 R. Döhrmann, S. Botta, A. Buffet, G. Santoro, K. Schlage, M. Schwartzkopf, S. Bommel, J. F. H. Risch, R. Mannweiler, S. Brunner, E. Metwalli, P. Müller-Buschbaum and S. V. Roth, *Rev. Sci. Instrum.*, 2013, **84**, 043901.
31 A. Paul, N. Paul, P. Müller-Buschbaum, A. Bauer and P. Böni, *J. Appl. Crystallogr.*, 2014, **47**, 1065–1076.
32 R. Lazzari, *J. Appl. Crystallogr.*, 2002, **35**, 406–421.
33 T. Salditt, T. H. Metzger, J. Peisl and G. Goerigk, *J. Phys. D: Appl. Phys.*, 1995, **28**, A236–A239.
34 R. Hosemann, *Polymer*, 1962, **3**, 349–392.
35 A. Hexemer and P. Müller-Buschbaum, Advanced grazing incidence techniques for modern soft matter materials analysis (feature article), *IUCrJ*, 2015, **2**, 106–125.
36 P. Müller-Buschbaum, in *Applications of Synchrotron Light to Scattering and Diffraction in Materials and Life Sciences*, ed. T. A. Ezquerra, M. C. Garcia-Gutierrez, A. Nogales and M. Gomez, Springer, Berlin, 2009, vol. 776, pp. 61–89.
37 G. Benecke, W. Wagermaier, C. Li, M. Schwartzkopf, G. Flucke, R. Hoerth, I. Zizak, M. Burghammer,

E. Metwalli, P. Müller-Buschbaum, M. Trebbin, S. Förster, O. Paris, S. V. Roth and P. Fratzl, *J. Appl. Crystallogr.*, 2014, **47**, 1797–1803.

38 E. Zillner, PhD Thesis, Freie University, Berlin, 2013, ISSN 1868-5781.

39 X. Peng, L. Manna, W. Yang, J. Wickham, E. Scher, A. Kadavanich and A. P. Alivisatos, *Nature*, 2000, **404**, 59–61.

40 C. S. S. Sandeep, J. M. Azpiroz, W. H. Evers, S. C. Boehme, I. Moreels, S. Kinge, L. D. A. Siebbeles, I. Infante and A. J. Houtepen, *ACS Nano*, 2014, **8**(11), 11499–11511.

41 E. Metwalli, V. Körstgens, K. Schlage, R. Meier, G. Kaune, A. Buffet, S. Couet, S. V. Roth and P. Müller-Buschbaum, *Langmuir*, 2013, **29**, 6331–6340.